Progress In Electromagnetics Research, PIER 100, 219–234, 2010

THREE-DIMENSIONAL NONLINEAR INVERSION OF ELECTRICAL CAPACITANCE TOMOGRAPHY DATA USING A COMPLETE SENSOR MODEL

R. Banasiak, R. Wajman, and D. Sankowski

Computer Engineering Department
Technical University of Lodz
Lodz, Poland

M. Soleimani

Department of Electronic & Electrical Engineering
University of Bath
Bath, UK

Abstract—Electrical Capacitance Tomography (ECT) is a non-invasive and non-destructive imaging technique that uses electrical capacitance measurements at the periphery of an object to generate map of dielectric permittivity of the object. This visualization method is a relatively mature industrial process tomography technique, especially in 2D imaging mode. Volumetric ECT is a new method that poses major computational challenges in image reconstruction and new challenges in sensor design. This paper shows a nonlinear image reconstruction method for 3D ECT based on a validated forward model. The method is based on the finite element approximation for the complete sensor model and the solution of the inverse problem with nonlinear iterative reconstruction. The nonlinear algorithm has been tested against some complicated experimental test cases, and it has been demonstrated that by using an improved forward model and nonlinear inversion method, very complex shaped samples can be reconstructed. The reconstruction of very complex geometry with objects in the shape of letters H, A, L and T is extremely promising for the applications of 3D ECT.

Corresponding author: M. Soleimani (m.soleimani@bath.ac.uk).

1. INTRODUCTION

In Electrical Capacitance Tomography (ECT) the internal permittivity distribution is computed based on the knowledge of the capacitance measurement between electrodes on the surface of the body [14, 16]. It is often assumed that the electric fields are confined to the 2D electrode plane, and the reconstruction is based on 2D assumptions. However, the electric field spreads out in three dimensions. Therefore, volumetric structures have significant effect on the reconstructed images [5, 9–11]. Electrodes at the surface of the volume apply an electrical potential into the surrounding area, and emergent charge is measured at the boundary. The measured data are then used in an electrostatic model to determine the dielectric permittivity properties of the object. Three dimensional ECT imaging is to become an important tool in industrial imaging for process monitoring [4, 7]. Much work has gone into the production of accurate forward models which describe the electrostatic forward model and inverse model, in order to efficiently recover images of the dielectric parameters [9–11]. In the past few years there has been a great deal of interest in using volumetric ECT both in 3D and in the dynamic imaging mode of 4D ECT [1, 8, 12]. A major challenge for moving from 2D to 3D capacitance tomography is the image reconstruction aspect of 3D ECT, especially in the case of the forward modeling. In [12], a linear forward model has been adapted by using the sensitivity matrix of an empty tank, which will pose some limitations in imaging results, regardless of the inversion algorithm. This paper focuses on the extension of 3D ECT image reconstruction using a nonlinear algorithm. For the inverse problem [17–23] several image reconstruction techniques have been developed [2, 3, 13, 15]. This paper adapts a nonlinear inversion algorithm for the image reconstruction. The problem of ECT image reconstruction is therefore two-fold. First, the model to describe the electrical field distribution within the area must be accurate, and second the inverse problem must be reliable at estimating the electrical properties within the imaging area. Numerical algorithms, based on the Finite Element Method (FEM) for the forward model, rely on the accurate definition of the volume and the mesh descretization being adequate for the calculation. It has been found that for an accurate forward model, the FEM mesh resolution must be of a high quality. This paper presents image reconstruction results of 3D ECT using a complete sensor model. A complete sensor model includes exterior screen, dielectric wall and the imaging region. A fully nonlinear iterative algorithm has been implemented, in which the forward problem is solved, and the 3D sensitivity map is updated in each iteration. Test examples chosen in this study are extremely

challenging, and marked improvement can be seen using nonlinear image reconstruction compared with using a linear algorithm.

2. EXPERIMENTAL SETUP

Three-dimensional capacitance sensor used in this study comprises of an array of conducting plate electrodes, which are mounted on the outside of a non-conducting pipe and surrounded by an electrical shield. For a metal wall pipe or vessel, the sensing electrodes must be mounted internally, with an insulation layer between the electrodes and the metal wall, using the metal wall as the electrical shield. Other components in the sensor include radial and axial guard electrodes, which are arranged differently to reduce the external coupling between the electrodes and to achieve improved quality of measurements and hence images.

The experimental setup in this work consists of a 32-electrode sensor of 304 mm of height and 150 mm in diameter, a novel 32-channel ECT measurement unit with fully programmable gains developed in Poland [6] (see Figure 1(a)) and a high performance PC with quad core CPU and 32 GB of RAM memory. The sensor is built according to the 3D ECT measurement concept, extending this to four planes with 8 electrodes on each plane. There are two boundary planes (1st and 4th) with the electrode height of 70 mm and two internal planes (2nd and 3rd) with the electrode height of 30 mm — see Figure 1(b). An electrode area asymmetry has been applied to keep a distant, inter-plane measurement signal detectable by a measurement unit.

The sensor structure includes a full shielding arrangement

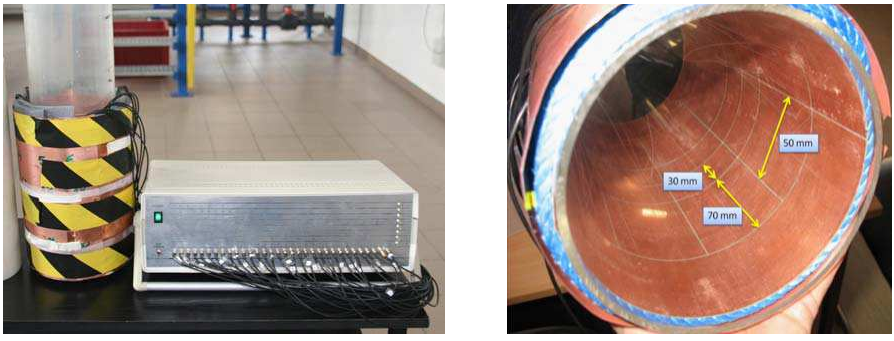

(a) (b)

Figure 1. (a) 3D ECT experimental setup, (b) 3D ECT sensor layout.

including a copper-made outer screen and boundary screens. The plexiglass-made (Polymethyl methacrylate) transparent pipe with a thickness of 4 mm has been used for the purpose of mounting the sensor — see Figure 1(b). The measurement strategy used in this paper is as follows: firstly, the excitation electrode has a positive potential while the rest of the remaining electrodes are grounded. Each electrode is used as an excitation electrode in turn. Consequently, $M = \frac{N \cdot (N-1)}{2}$ independent measurements are acquired for a sensor with N electrodes. In comparison to the classical 2D ECT approach [16], the 3D measurements are also performed between electrodes from different layers, providing true spatial information about the imaging object. A more detailed description of the measurement system can be seen in [6].

3. THE FORWARD MODEL FOR 3D CAPACITANCE TOMOGRAPHY AND ITS VALIDATION

The forward problem for 3D capacitance tomography is the simulation of measurement data for a given value of excitation and material permittivity distribution. The inverse problem is the imaging result for a given set of measurement data. To solve the inverse problem the forward problem need to be solved. In a simplified mathematical model, the electrostatic approximation $\nabla \times E = 0$ is taken, effectively ignoring the effect of wave propagation. Let's take $E = -\nabla u$ and assume no internal charges. Then the following equation holds:

$$\nabla \cdot \varepsilon \nabla u = 0 \text{ in } \Omega \tag{1}$$

where u is the electric potential, ε is dielectric permittivity and Ω represents the region containing the field. The potential on each electrode is known as:

$$u = v_k \text{ at } e_k \tag{2}$$

where e_k is the k-th electrode held at the potential v_k. Using the FEM method [10] we obtain:

$$\mathbf{K}(\varepsilon)\mathbf{U} = \mathbf{B} \tag{3}$$

where the matrix $\mathbf{K}$ is the discrete representation of the operator $\nabla \cdot \varepsilon \nabla$, the vector $\mathbf{B}$ is the boundary condition term and $\mathbf{U}$ is the vector of electric potential solution. The electric current on the k-th electrode is given by:

$$I_k = \int\limits_{E_k} \varepsilon \frac{\partial u}{\partial n} dx^2 \tag{4}$$

where n is the inward normal on the k-th electrode. To calculate simulated capacitance data the forward model of the 3D capacitance

sensor has to be developed. There have been some attempts in forward modelling of 3D ECT [9–12] but most of them seem to be too simple and do not reflect actual capacitance sensor structure. As a result they cannot provide as accurate simulation data.

In this paper, a novel complete forward sensor model has been developed to improve the accuracy of the forward solution. The main advantage of the new complete sensor idea is to simulate some important sensor parts like an internal and external screening system, an isolation area and a mounting pipe profile. This idea can be seen in Figure 2. The complete sensor forward model has been developed in our own FEM software for 3D ECT [9, 10]. It has been composed of three main layers: a sensor interior layer, a mounting pipe layer and an insulation area layer. The layers have been meshed using different mesh density to improve the accuracy of the forward model for the neighbouring electrodes.

The dimensions of the forward model of the experimental 3D ECT sensor have been applied according to its real dimensions. There were two meshes with different complexity, developed to avoid an inverse crime issue. The forward mesh for a complete sensor model has been composed of 79,232 nodes and 447,385 elements. The inverse mesh for non-linear reconstruction has been composed of 22,640 nodes and 114,139 elements. The experimental validation of the forward model has been done using three numerical models: a simple model, a screened-only model and a full complete model. The simple forward model of the 3D ECT sensor was built using a one-layered mesh (imaging layer) with uniform internal element densities. Electrodes were simulated on the outer surface of the mesh. The simple model did not include the screens arrangement, the insulation area or the mounting pipe region. The screened-only model was composed of two layers: the internal layer (imaging layer) with simulated electrodes

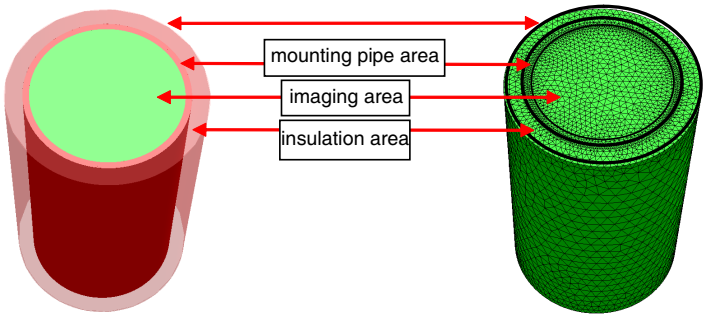

Figure 2. The complete forward model meshing.

and the external layer with an outer surface acting as a screen. The screened-only model did not include boundary screens, the insulation area or the mounting pipe simulation. In screened-only forward model, mesh density of the internal and the external layers are different. The complete forward model has been composed of three layers with different mesh densities: the internal layer (imaging layer) with simulated electrodes, the mounting pipe layer and the insulation layer with an outer screen. The internal structures of all models are presented in Figure 3.

For the validation purpose, three different permittivity distributions have been generated experimentally and in simulated models. In this paper, the normalisation of simulated capacitance data has been done according to the formula:

$$\mathbf{C}_{norm} = \frac{(\mathbf{C}_{\text{exp}} - \mathbf{C}_{low})}{(\mathbf{C}_{high} - \mathbf{C}_{low})} \tag{5}$$

where $\mathbf{C}_{norm}$ is the normalised capacitance, $\mathbf{C}_{\text{exp}}$ is the absolute capacitance measured, $\mathbf{C}_{low}$ is absolute capacitance when the imaging area is filled with material with low permittivity, and $\mathbf{C}_{high}$ is absolute capacitance when the imaging area is filled with material with high permittivity. The normalisation acts as a calibration process and results in an improved signal to noise ratio compared to absolute measured data. Both simulated and experimental capacitance data are normalised. First, validation process has been done for the simple example of the symmetrical permittivity distribution (Phantom A). Phantom A includes a 50 mm diameter rod made from ertalon with relative permittivity $\varepsilon_r = 3.0$, located in the centre of the sensor area, with the air ($\varepsilon_r = 1.0$) as a background. For the purpose of comparison, the electrode number 1 is an excitation electrode and 31 measurement of this excitation has been considered. Figure 4 shows results of forward modelling using three different 3D ECT forward models and the Phantom A.

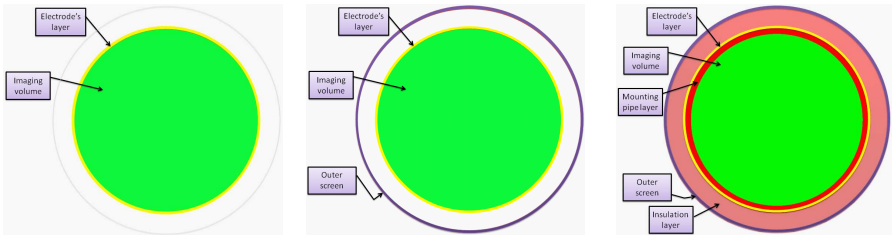

Figure 3. The cross-section of three validated 3D ECT forward models.

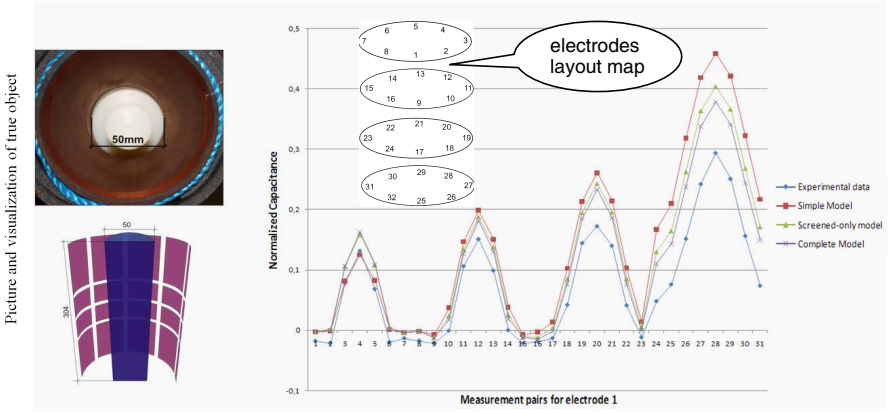

Figure 4. Validation results for the Phantom A.

All forward model show relatively good matching between experimental and simulated data. The advantage of the complete forward model can be seen for measurements between electrodes that are far away from each other, especially for the inter-plane measurements (measurements No. 10–31). The best data matching using the complete forward model can be achieved when the measurement is done using the 1st and 4th planes of the capacitance sensor (measurement No. 28). It means that the simple forward model is not accurate enough when the measurement is performed using the most distant electrodes and results in a large numerical error. Generally, both screened-only and complete forward models provided noticeably less error and better data matching. To further investigate the forward validation, two more complicated sets of simulated and experimental capacitance data have been compared. In Phantom B, an air hole with a diameter of 50 mm localized in the centre of the 3D ECT sensor with ertalon acting as a background. The third testing phantom (Phantom C) is the most difficult example due to its axial asymmetry. In this case the sensor volume had been filled with a high permittivity (ertalon) up to half of its height (152 mm). The remaining volume of the sensor had been filled in the same way as Phantom B. The numerical models of these phantoms have been built according to their geometry and electrical properties. The validation results obtained can be seen in Figure 5 and Figure 6.

The simulated forward model shows that the simple model is not accurate for the neighbouring electrodes and inter-plane measurements as can be seen in Figure 5 and Figure 6. This is a similar observation obtained from Phantom A. The simple forward model usually results

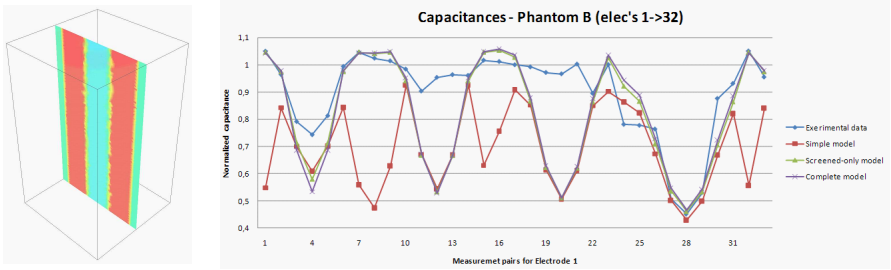

Phantom B Validation

Figure 5. Validation results for the Phantom B.

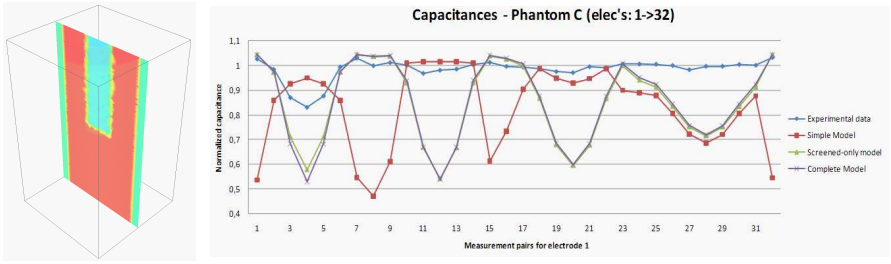

Phantom C Validation

Figure 6. Validation results for the Phantom C.

in a large mismatching between simulated and experimental data. The screened-only forward model and the complete forward model provided better matching for most of measured data. There are still a number of mismatched capacitance data which may affect the nonlinear reconstruction efficiency, especially for some inter-plane capacitance measurements. To estimate the difference between simulated and experimental data, the residual capacitance error has been calculated according to the formula:

$$\delta rc = \frac{||\mathbf{C}_m - \mathbf{C}c||}{||\mathbf{C}_m||} \tag{6}$$

where $\mathbf{C}_m$ represents the real normalized measured data and $\mathbf{C}c$ represents the measurement data calculated as a normalized solution of the forward simulation process. The residual capacitance error is shown in Table 1.

The values of residual capacitance error presented in Table 1 show the difference in accuracy ECT forward model. The value of Δrc can also represent the minimal error, which nonlinear reconstruction can achieve. Due to severely ill-posed nature of the inverse problem in

Table 1. Residual capacitance error between experimental and simulated data using Phantom B and Phantom C and three types of 3D ECT forward models (simple, screened-only and complete).

	Simple model	Screened-only model	Complete model
Δrc_B	0.31	0.21	0.19
Δrc_C	0.27	0.16	0.14

ECT a very small error in measured data (or simulation) can cause a large error in image reconstruction. Similarly a small improvement in forward modelling may help to make image reconstruction more accurate and robust. This is even more important when a nonlinear image reconstruction is used and small objects and challenging shapes are reconstructed. Screen-only and complete model are both showing improvement in estimation of the forward model that suggest the importance of modelling the exterior shielding. Bothe of these will require solving forward model that are larger in mesh size than the simple forward model, but very close to each other in terms of complexity of the forward modelling. For these reasons the complete sensor model has been selected as a method of choice for the image reconstruction.

4. SENSITIVITY ANALYSIS

To obtain sensitivity distribution inside the sensor volume the Fréchet derivative of the measured capacitance is calculated with respect to a perturbation in the permittivity. A simple approach is to ignore the higher order terms. This can simply be extended to a formal proof using an operator series, and a derivation of the sensitivity formula has been given in [9, 10, 12]. To get the change in charge Q on electrode E_i when E_j is excited, the potential u_i is applied when electrode E_i is driven and potential u_j *applied* when E_j is driven. The sensitivity formula is as follows:

$$\delta Q_{ij} = \int_{\Omega_p} \delta\varepsilon \nabla u_i \cdot \nabla u_j dx^3 \tag{7}$$

where Ω_p represents the perturbed region. Here u_i and u_j can be calculated by solving the forward problem when electrodes i and j are excited. Formula of Equation (7) provides an efficient method to calculate the sensitivity map and the Jacobian matrix, as the results of electric potential in interior is already available due to the forward modelling.

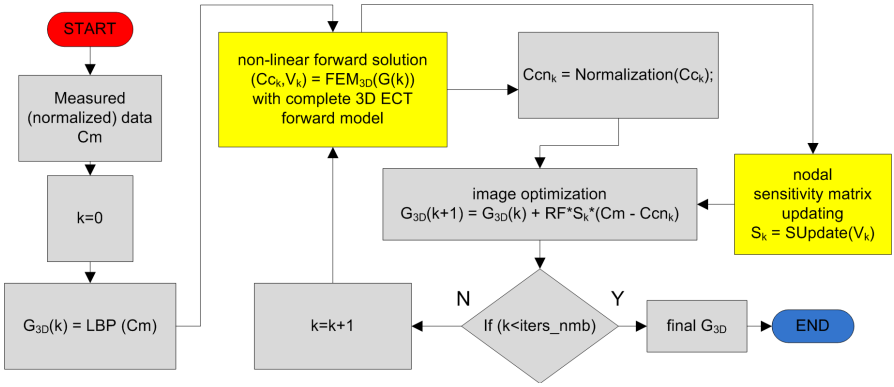

Figure 7. Flowchart of the level set reconstruction algorithm.

5. NONLINEAR RECONSTRUCTION ALGORITHM

The main goal of an inverse problem solution is to approximate the permittivity distribution inside of the sensor volume using capacitance data. In order to find an approximate 3D inverse solution, an iterative back-projection algorithm has been implemented in a fully-nonlinear scheme — see flow chart of the algorithm in Figure 7.

The first step of is to find an initial image $\mathbf{G}_{3D}(0)$ using measured data $\mathbf{C}_m$ and a linear back-projection (LBP) method with sensitivity matrix $\mathbf{S}_0$ calculated for homogeneous media. In this paper, a simulated homogeneous permittivity distribution with ($\varepsilon_r = 2.0$) has been applied for the calculation of $\mathbf{S}_0$. The value of the dielectric constant has been selected according to the known high ($\varepsilon_r = 3.0$) and low ($\varepsilon_r = 1.0$) value of permittivity for test objects. The next step is to find a nonlinear forward solution $\mathbf{C}c_0$ and $\mathbf{V}_0$ using the complete forward model for the initial image $\mathbf{G}_{3D}(0)$, where $\mathbf{C}c_0$ is a calculated measurement data and $\mathbf{V}_0$ is an electrical field distribution. At this stage a new sensitivity matrix can be recalculated. The image $\mathbf{G}_{3D}(k)$ in k-th iteration can be updated using various optimisation methods [9, 12, 13, 15, 16]. A k-th step image reconstruction includes solving a forward problem for $\mathbf{V}_k$ and $\mathbf{C}c_k$, and the sensitivity matrix $\mathbf{S}_k$ and updating permittivity. For convenient a linear back-projection is used for updating permittivity in each nonlinear iteration. The convergence of the image reconstruction can be adjusted by the relaxation factor RF. In this paper the RF factor has been chosen empirically from the value range: 0.3–2 and resulted in satisfactory convergence of the algorithm (see Figure 10).

true object

(a)

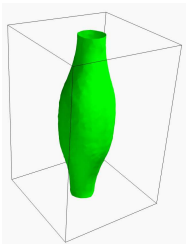

linear back-projection

(b)

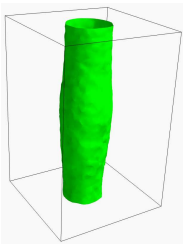

iterative nonlinear reconstruction with 10 iterations and RF=1.5;

(c)

Figure 8. 3D image reconstruction of a cylindrical-shaped test phantom where (a) is a picture of the true object, (b) is a linear back-projection based 3D image, (c) is a nonlinear reconstruction based 3D image.

6. RESULTS AND DISCUSSION

Both a linear back-projection and non-linear reconstruction iterative algorithm have been applied to the static experimental data that had been acquired for the relatively simple symmetric permittivity distribution, as depicted in Figure 8(a).

Figures 8(b) and 8(c) show the comparison between linear and nonlinear image reconstruction methods. It can be seen that the linear back-projection is not able to resolve a proper shape of a real experimental object, mainly due to the fact that the sensitivity matrix has been calculated for uniformly distributed media. The shape obtained by one-step LBP technique is irregular in the axial direction and demonstrates the weakness of homogeneous permittivity distribution based sensitivity maps in the centre of the 3D ECT sensor. Advantage of the iterative nonlinear reconstruction technique can be easily seen in Figure 8(c), where the cylindrical-shaped object has been resolved and localized properly. In that case, the non-linearity of the iterative process has been considered by updates of the sensitivity maps. Due to good experience and promising results obtained for a simple symmetrical experimental phantom, another four challenging static letter-shaped test phantoms (T-shaped, H-shaped, L-shaped and A-shaped) have been developed and reconstructed using both the linear and non-linear reconstruction technique. The letters are made of material with relative permittivity of 3.0. The non-linear reconstruction of these objects has been performed using both the complete forward model mesh and inverse mesh in the iterative scheme with 50 iterations. One iteration took about 588 seconds and the

final image was completed after 6 hours using two quad-core Intel Xeon CPU's with 2.33 GHz and 16 GB of RAM memory. All the computations have been done using Matlab code and the multi-core parallel computing scheme has been used during the reconstruction process. The results of a 3D image reconstruction of letter-shaped phantoms have been presented in Figure 9.

The obtained results show great potential for reducing the non-linearity effect of the 3D ECT inverse problem by using a newly

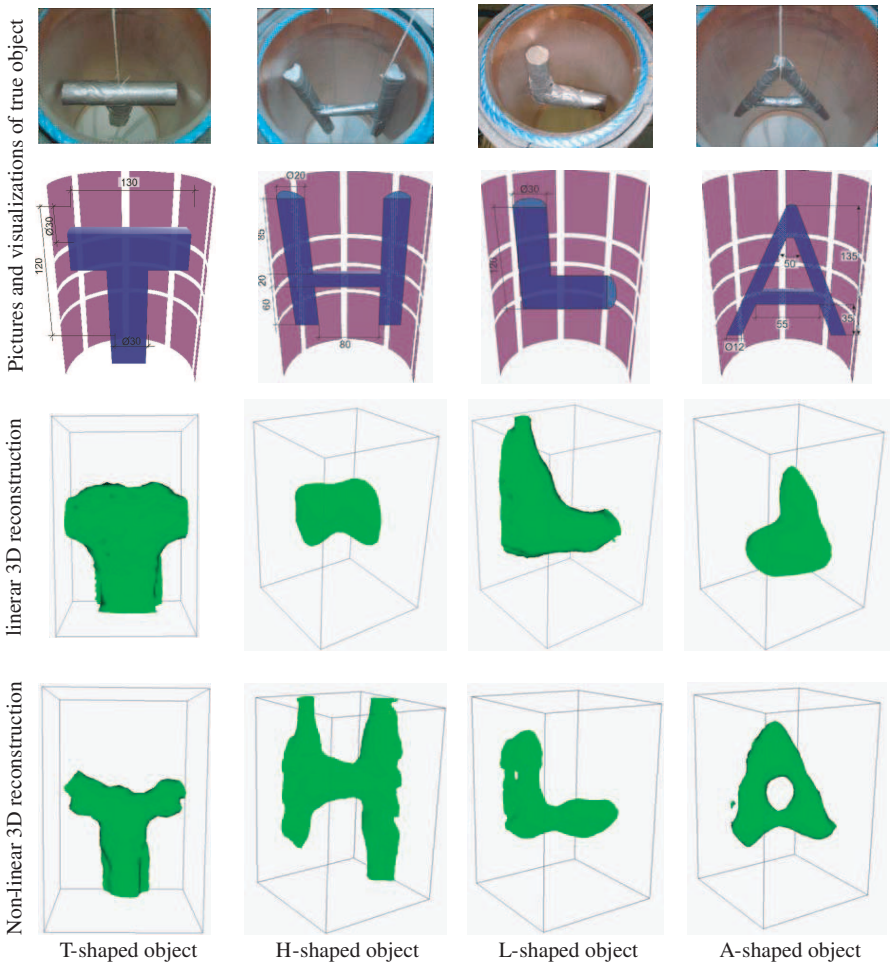

Figure 9. The results of 3-dimensional reconstruction of letter-shaped objects using both: linear and non-linear reconstruction method.

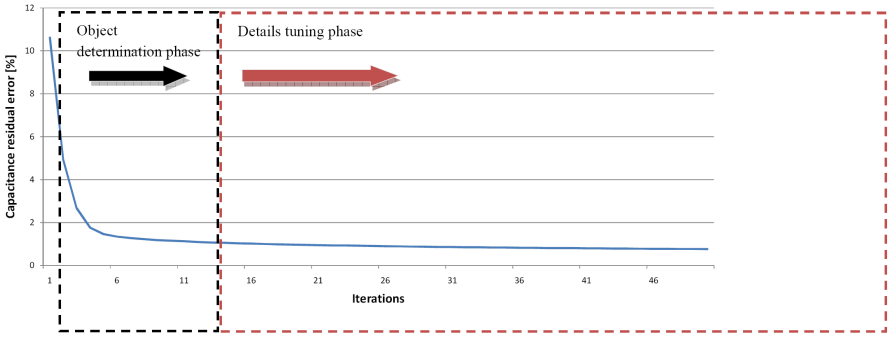

Figure 10. The convergence graph showing the nonlinear reconstruction progress and its two main phases during 50 iterations for the L-shaped object.

developed and accurate 3D ECT forward model, and updates of the sensitivity maps. Only the L-shaped phantom reconstruction can be identified as a true L-shaped object using the linear reconstruction technique. As it expected the T-, L- and A-shaped objects were not resolved properly with LBP method. The non-linear reconstruction identified H-shaped and A-shaped objects with remarkably good image quality. The good efficiency of the nonlinear reconstruction algorithm can be observed with the most challenging test of the A-shaped phantom. The A-shaped letter was reconstructed with good details, including the interior horizontal bridge and a small hole — which appears to be a real achievement for a low resolution capacitive imaging system. For all the letter-shaped test phantoms, the residual capacitance error has been reduced during the nonlinear reconstruction process. The main part of the 3D image reconstruction is completed within 6–10 iterations. Therefore the non-linear iterative reconstruction may be considered as a two-step process where the first 5–15 iterations determine an approximate spatial permittivity distribution of a true object, and afterwards the details of the object can be detected and tuned during the next 20–30 iterations. The convergence graph for 50 iterations of nonlinear reconstruction of the L-shaped object is presented in Figure 10. The convergence rate has been measured by percentage of residual capacitance error.

7. CONCLUSIONS

This paper proposes a finite element-based method using a complete sensor model for the reconstruction of three-dimensional permittivity

distributions. The proposed method is based on the so-called complete sensor model that takes into account all geometrical aspects of the ECT sensor. Both the forward and inverse problems are discussed, and the results from challenging test examples with real measurement data are given. It is shown that in phantom experiments with accurate finite element computations, it is possible to obtain static images from complex shaped structures. In order to obtain more accurate images it may be useful to increase the number of electrode planes and also the number of electrodes on each plane. In ECT this is particularly difficult because to increase the number of electrodes, we need to decrease the size of each electrode, which will result in smaller capacitance data. Improving the accuracy of the reconstructed image is important as it makes it possible to extract more information from the imaging system. The nonlinear inversion method proposed here, using a validated forward model is one way to improve the accuracy of reconstructed images, with an obvious increase in the computational time of the image reconstruction. The complete sensor model presented here improves the accuracy of the forward validation, especially the validation of measurement data from neighboring electrodes, which is generally harder. In our continued effort we will work on improving computational efficiency of the algorithm as well as further improvement in accuracy of the forward modeling. The complicated experimental tests presented here, show a great deal of potential for 3D ECT in its future applications. This makes the 3D ECT as an exciting new research front in industrial process tomography with scope for more innovations in computational aspect of the 3D ECT research.

ACKNOWLEDGMENT

This work is funded by the European Community's Sixth Framework Programme — Marie Curie Transfer of Knowledge Action (DENIDIA, contract No.: MTKD-CT-2006-039546). The work reflects only the author's views, and the European Community is not liable for any use that may be made of the information contained therein.

REFERENCES

1. Banasiak, R., R. Wajman, and M. Soleimani, "An efficient nodal Jacobian method for 3D electrical capacitance image reconstruction," *Insight — Non-destructive Testing and Condition Monitoring*, Vol. 51, No. 1, 36–38, 2009.
2. Calderon, A. P., "On an inverse boundary value problem," *Seminar on Numerical Analysis and Its Applications to Continuum*

Physics (Rio de Janeiro), 65–73, Sociedade Brasileira de Matematica, 1980.

3. Cheney, M., D. Isaacson, and J. C. Newell, "Electrical impedance tomography," *SIAM Review*, Vol. 41, No. 1, 85–101, 1999.
4. Dyakowski, T., L. F. C. Jeanmeure, W. B. Zimmerman, and W. Clark, "Direct flow-pattern identification using electrical capacitance tomography," *Experimental Thermal and Fluid Science*, Vol. 26, No. 6–7, 763–773, 2002.
5. Nurge, M. A., "Electrical capacitance volume tomography with high contrast dielectrics using a cuboid sensor geometry," *Measurement Science and Technology*, Vol. 18, No. 5, 1511–1520, 2007.
6. Olszewski, T., P. Brzeski, J. Mirkowski, A. Plaskowski, W. Smolik, and R. Szabatin, "Modular capacitance tomograph," *Proc. of 4th International Symposium on Process Tomography*, Warsaw, 2006.
7. Romanowski, A., K. Grudzien, R. Banasiak, R. A. Williams, and D. Sankowski, "Hopper flow measurement data visualization: Developments towards 3D," *Proc. of 5th World Congress on Industrial Process Tomography*, Bergen, Norway, 2006.
8. Soleimani, M., C. N. Mitchell, R. Banasiak, R. Wajman, and A. Adler, "Four-dimensional electrical capacitance tomography imaging using experimental data," *Progress In Electromagnetics Research*, PIER 90, 171–186, 2009.
9. Soleimani, M., "Three-dimensional electrical capacitance tomography imaging," *Insight — Non-destructive Testing and Condition Monitoring*, Vol. 48, No. 10, 613–617, 2006.
10. Wajman, R., R. Banasiak, Ł. Mazurkiewicz, T. Dyakowski, and D. Sankowski, "Spatial imaging with 3D capacitance measurements," *Measurement Science and Technology*, Vol. 17, No. 8, 2113–2118, August 2006.
11. Warsito, W. and L. S. Fan, "Development of 3-dimensional electrical capacitance tomography based on neural network multicriterion optimization image reconstruction," *Proc. of 3rd World Congress on Industrial Process Tomography*, Str. 942–947, Banff, 2003.
12. Warsito, W., Q. Marashdeh, and L. S. Fan, "Electrical capacitance volume tomography," *IEEE Sensors Journal*, Vol. 7, No. 3–4, 525–535, 2007.
13. Warsito, W. and L. S. Fan, "Neural network based multicriterion optimization image reconstruction technique for imaging two- and three-phase flow systems using electrical capacitance

tomography," *Measurement Science and Technology*, Vol. 12, 2198–2210, 2001.

14. Williams, R. A. and M. S. Beck, *Process Tomography, Principles, Techniques and Applications*, Butterworth-Heinemann, Oxford, UK, 1995.
15. Yang, W. Q., D. M. Spink, T. A. York, and H. McCann, "An image-reconstruction algorithm based on Landweber's iteration method for electrical-capacitance tomography," *Measurement Science and Technology*, Vol. 10, 1065–1069, 1999.
16. Yang, W. Q. and L. Peng, "Image reconstruction algorithms for electrical capacitance tomography," *Measurement Science and Technology*, Vol. 14, R1–R13, 2003.
17. Goharian, M., M. Soleimani, and G. Moran, "A trust region subproblem for 3D electrical impedance tomography inverse problem using experimental data," *Progress In Electromagnetics Research*, PIER 94, 19–32, 2009.
18. Chen, G. P., W. B. Yu, Z. Q. Zhao, Z. P. Nie, and Q. H. Liu, "The prototype of microwave-induced thermo-acoustic tomography imaging by time reversal mirror," *Journal of Electromagnetic Waves and Applications*, Vol. 22, No. 11–12, 1565–1574, 2008.
19. Cheng, X., B. I. Wu, H. Chen, and J. A. Kong, "Imaging of objects through lossy layer with defects," *Progress In Electromagnetics Research*, PIER 84, 11–26, 2008.
20. Huang, C. H., Y. F. Chen, and C. C. Chiu, "Permittivity distribution reconstruction of dielectric objects by a cascaded method," *Journal of Electromagnetic Waves and Applications*, Vol. 21, No. 2, 145–159, 2007.
21. Franceschini, G., M. Donelli, D. Franceschini, M. Benedetti, P. Rocca, and A. Massa, "Microwave imaging from amplitude-only data-advantages and open problems of a two-step multi-resolution strategy," *Progress In Electromagnetics Research*, PIER 83, 397–412, 2008.
22. Chen, X. D., "Subspace-based optimization method in electric impedance tomography," *Journal of Electromagnetic Waves and Applications*, Vol. 23, No. 11–12, 1397–1406, 2009.
23. Polydorides, N., "Linearization error in electrical impedance tomography," *Progress In Electromagnetics Research*, PIER 93, 323–337, 2009.